Lab on a Chip

Multi-curvature micropatterns unveil distinct calcium and mitochondrial dynamics in neuronal networks

Journal:	*Lab on a Chip*
Manuscript ID	LC-ART-11-2020-001205.R1
Article Type:	Paper
Date Submitted by the Author:	14-Jan-2021
Complete List of Authors:	Khan, Hammad; Montana State University Bozeman, Electrical and Computer Engineering Beck, Connor; Montana State University Bozeman, Electrical and Computer Engineering Kunze, Anja; Montana State University Bozeman, Electrical and Computer Engineering

Multi-curvature micropatterns unveil distinct calcium and mitochondrial dynamics in neuronal networks

Hammad Khan[a], Connor Beck[a], Anja Kunze*[a,b]

[a]Department of Electrical and Computer Engineering, Montana State University, Bozeman, Montana 59717, USA. Email: anja.kunze@montana.edu

[b]Montana Nanotechnology Facility, Montana State University, Bozeman, Montana 59717, USA.

Tangential curvatures are a key geometric feature of tissue folds in the human cerebral cortex. In the brain, these smoother and firmer bends are called gyri and sulci and form distinctive curved tissue patterns imposing a mechanical stimulus on neuronal networks. This stimulus is hypothesized to be essential for proper brain cell function but lacks in most standard neuronal cell assays. A variety of soft lithographic micropatterning techniques can be used to integrate round geometries in cell assays. Most microfabricated patterns, however, focus only on a small set of defined curvatures. In contrast, curvatures in the brain span a wide physical range, leaving it unknown which precise role distinct curvatures may play on neuronal cell signaling. Here we report a hydrogel-based multi-curvature design consisting of over twenty bands of distinct parallel curvature ranges to precisely engineer neuronal networks' growth and signaling under patterns of arcs. Monitoring calcium and mitochondrial dynamics in primary rodent neurons grown over two weeks in the multi-curvature patterns, we found that static calcium signaling was locally attenuated under higher curvatures ($k > 0.01\ \mu m^{-1}$). In contrast, to randomize growth, transient calcium signaling showed higher synchronicity when neurons formed networks in confined multi-curvature patterns. Additionally, we found that mitochondria showed lower motility under high curvatures ($k > 0.01\ \mu m^{-1}$) than under lower curvatures ($k < 0.01\ \mu m^{-1}$). Our results demonstrate how sensitive neuronal cell function may be linked and controlled through specific curved geometric features. Furthermore, the hydrogel-based multi-curvature design possesses high compatibility with various surfaces, allowing a flexible integration of geometric features into next-generation neuro devices, cell assays, tissue engineering, and implants.

Introduction

The architecture of the human cerebral cortex displays a folded landscape having evolved and expanded tangentially across a spherical surface to optimize brain surface area within the human skull[1-3]. This tissue folding process starts during the fetal developmental stage and plays a crucial role as the brain matures and creates new neuronal connections [4-8]. Aside from the deeply folded landscape, abnormal cortical folding has been associated with neurological, cognitive, and behavioral disorders such as epilepsy[9],

autism[10, 11], and schizophrenia[12-14]. Current computational-based evidence supports the hypothesis that forces get generated within cortical folds and impact cellular morphology and migration during cortical development[15]. However, how the cortical folds can result in bent neurite network growth and alter neuronal cell function remains poorly understood. From histological images[1, 15] two main curvature regions can be identified based on smaller ($0.001\ \mu m^{-1} < k < 0.008\ \mu m^{-1}$) and larger bends ($0.01\ \mu m^{-1} < k < 0.05\ \mu m^{-1}$, Fig. 1a). Various surface geometry modifying techniques such as microchannels[16], micropillars[17, 18], microfibers[19, 20], patterned substrate coatings[18, 21-25], or hydrogels[26-28] have been employed to guide the growth and orientation of neuronal cells from the peripheral and central nervous system[29]. Characteristic bending of neurite outgrowth based on curvatures has been explored by Smeal *et al.* on microfiber filaments using dorsal root ganglions (DRG)[19, 20], and by Roth *et al.* on poly-l-lysine (PLL) patterns using mouse neurons[25]. With microfiber filaments varying in their curvatures from 0.004 μm^{-1} to 0.06 μm^{-1}, Smeal *et al.* found that the highest curvature filaments had the strongest DRG neurite growth guidance effect. Roth *et al.* demonstrated further that curvatures above 0.1 μm^{-1} inhibited neurite outgrowth[25]. Beyond neurite growth, a ring-shaped surface pattern with curvature below 0.01 μm^{-1} has been used to demonstrate connected evoked calcium activity in small-scale neuronal networks grown from cortical neurons[23]. Although all these microenvironmental cues play an important role in neuronal outgrowth[29], how different curvature ranges drive functional spontaneously occurring neuronal behavior is still poorly understood. Hence, we designed a multi-curvature based micropattern to investigate how different curvature ranges influence spontaneously occurring transient calcium signaling events and mitochondrial transport in primary cortical neurons. Inspired by hydrogel soft-embossing methods[28, 30], we fabricated a range of curvatures ($k = 0.003 – 0.2\ \mu m^{-1}$) in a highly parallelized manner. Using our multi-curvature patterns, we studied the cellular response of rodent cortical neurons by analyzing how neurons grow their networks, how calcium (Ca^{2+}) fluorometry changes, and how mitochondrial transport gets impacted under distinct curvature ranges. Our results indicate that distinct curvature ranges leave a unique fingerprint of neuronal network behavior based on calcium signaling and mitochondria dynamics.

Materials and methods

Design and fabrication of multi-curvature micropatterns for neuronal cell assay using a hydrogel substrate

In figure 1b and 1c, the materials, the assembly, and the design of the multi-curvature micropatterns are shown. Through varying the number, the width, and the gap between the growth rings, six different designs were chosen. (Fig. 1d, growth ring = cells), leading into multi-curvatures ranging from 0.003 μm^{-1} to 0.2 μm^{-1} (Fig. 1e). A photolithography mask was designed using CleWin (PhoeniX, Netherlands) as a negative pattern to fabricate the multi-curvature micropatterns. KMPR 1050 (Microchem) was spin-

coated (500 rpm for 10 s ramp-up speed; 3000 rpm for 30 s; 1000 rpm, 10 s ramp down speed) and soft-baked at 100 °C for 15 min to obtain a feature height of 50 µm. The features were exposed (700 mJ/cm^3) to ultra-violet light using a contact aligner (Shipley SPR 1813) and developed (SU-8 developer) for 3.7 min followed by a thorough rinse with deionized (DI) water. Silicone elastomer base and curing agent (Sylgard) were mixed using a 10:1 base/curing agent ratio and poured onto the KMPR master wafer to cast the PDMS stamp. The PDMS elastomer mixture was cured for 2 h at 60 °C for rapid crosslinking and gently peeled off from the master and cut to size (Fig. 2a). For the fabrication of soft-gel features, a mixture of 3% w/v Type VII-A agarose (> 250 mg/cm^2) was heated in a convection oven at 80 °C. We chose this agarose concentration based on testing of agarose hydrogel repellant properties (Figure S1a and S1b). The liquid agarose solution was directly pipetted onto a Petri dish pre-coated with poly-d-lysine (PDL). After pipetting, the PDMS stamp was pressed firmly onto the agarose gel inspired by a previous method[27, 30]. Contact was maintained for 5 min, followed by a cooling period for 30 min before the PDMS stamp was removed. Feature integrity of the multi-curvature patterns was imaged using upright bright-field and inverted DIC-contrast microscopy at each fabrication step (Fig. 2b). To measure the swelling characteristic of agarose hydrogel, *in situ* imaging was utilized by loading the agarose with fluorescent microparticles (diameter: 15 µm, Bangs Lab). The position of the fluorescent microparticles was then imaged in 10 min intervals for 48 h (Fig. S2a) for subsequent particle image velocimetry (PIV). The image sequence was post-processed using the PIV module in MATLAB (Fig. S2b), resulting in particle displacement maps over time (Fig. S2c-e).

Cortical neuron cell culture

Rat embryonic brains (E18, BrainBits) were dissected following a previously established protocol[31-33]. Briefly, cortical tissues were dissociated in 10% (v/v) papain (Carica papaya, Roche) in Hibernate-E (BrainBits) at 37 °C for 15 min. Dissociated cortical neurons were centrifuged (6 min, 600 rpm, at room temperature) and then seeded at a concentration of 250,000 cells/ml per device. Cortical neurons were incubated (95% air, 5% CO_2, 37 °C) in standard neuronal culture media (97% (v/v) Neurobasal Plus Medium (Gibco), B-27 Plus Supplement with 2% (v/v) (Gibco), and 1% (v/v) penicillin-streptomycin (Gibco)) and grown for over two weeks (3DIV, 9 DIV, 12 DIV, 15 DIV = days *in vitro*). The growth of neurite networks was then quantified in each growth ring using a mask during image-post processing (Fig. 2d-2e).

Mitochondria and calcium labeling

Day 12-15 cortical neurons were incubated with red mitochondria tracking dye (1.88 µM, MitoTracker Red CMXRos, Invitrogen) mixed into standard media culture (0.02% v/v) and incubated for 1 h. The

neuronal culture was gently washed with pre-warmed imaging media (98% (v/v) Neurobasal Plus without Phenol Red, 2% (v/v) B-27 Supplement, Gibco) before imaging. To achieve proper staining of the culture, the MitoTracker was introduced first, imaged, and followed by Fluo-4 AM calcium staining with gentle washing in-between. For calcium labeling, Fluo-4 AM direct calcium assay kit (Invitrogen) was prepared following the manufacturer's protocol with probenecid acid (10 mM). The final Fluo-4 AM mixture was added to neuronal cultures in a 1:1 ratio with media and incubated for 1 h.

Live-cell imaging

Cortical neuron cultures were live imaged using an inverted imaging system (Leica DMi8S) with white-light bright-field, phase-contrast, or differential interference contrast (DIC) starting at day three *in vitro* (DIV). Spontaneous (activity-independent) transient calcium signals were captured in live cortical neuron cultures using a single-wavelength calcium indicator Fluo-4 AM (see supplementary video file 1) due to its wide dynamic range, easy to use, and wide range of comparable studies in the field of calcium imaging[6, 34-36]. Live-cell fluorescent calcium dynamics in Fluo-4 AM labeled neurons were captured using the same microscope fluorescent settings (Leica DMi8S, GFP filter, 20x air) with channel exposure set to 250 ms. Transient fluorescent calcium signals were recorded for 50 s at 2 fps (2 Hz). Separate static fluorescent calcium signals were captured based on a single-image setting. Live-cell imaging of fluorescently labeled mitochondria was taken at 2 fps for 120 s using the same microscope (Leica DMi8S, TxRed filter, 20x air)

Image processing and analysis

Static calcium profiling

Image processing of static calcium profiles was done through ImageJ using a custom-written semi-automated calcium profiling plugin (Fig S4a, S4b). Intensity signals were projected to a radial line with its origin in the micropattern's center. The radial line then automatically scans the entire micropattern region clockwise, and yields mean and SE intensity profiles. The projected intensity profile (I) was then normalized based on the number of cells (N_{cell}) in each ring and based on the average intensity (I_{avg}) over the whole image (Eq.1, eq. 2, Fig. S4d). The curvature for each concentric circle (k) is the inverse of its radius (r) starting from the center of the micropattern (Eqn. 3). The resulting normalized calcium intensity (I^*) is then used to compare differences in the multi-curvature micropatterns based on different arcs in the neuronal network (Fig. S4e).

$$I_{cell} = \frac{I}{N_{cell}} \#(1)$$

$$I^* = \frac{I_{cell}}{I_{avg}} \#(2)$$

$$k = \frac{1}{r} \#(3)$$

Transient calcium fluorometry

The transient live-cell calcium signaling data based on spontaneously active cell bodies with neurites were analyzed using custom algorithms in MATLAB inspired by *Ikegaya et al.* [6, 37]. Exported microscope videos were imported into MATLAB and treated as sequences of images. The image sequence was then segmented into regions of interest (ROIs) using an auto-detection algorithm. Individual cell bodies were segmented into ROIs and indexed with a number and a radius code corresponding to the center of the multi-curvature micropattern. The ROIs were then sorted into radius groups corresponding to distinct curvature regions (Fig. S5a). Mean fluorescent intensity for each ROI was extracted over the time series, and a numerical derivative was computed for each transient wave ($\Delta F/\Delta t$) based on a similar algorithm reported in Beck *et al.* [31]. Calcium events based on increasing cytosolic calcium levels were denoted as a spike for visualization where the numerical derivative exceeded 2.5 times the standard deviation. The spike rate of calcium events was then computed as the average number of calcium increase events per second for each ROI (Fig S5b).

Synchronous calcium network identification

To quantify synchronous events of calcium increase inspired by *Ikegaya et al.* [37], we measured the overall signal synchronicity in the cortical network through calculating a synchronicity index (SI) from the raster plots showing increase in calcium events. Spike raster plots were compared using the Sørensen–Dice similarity coefficient[31]. Unique comparisons (i.e., a 3-length ROI index would follow as ROI_1-ROI_2, ROI_1-ROI_3, ROI_2-ROI_3) was then linearized and run through the filter function (Eq. 4) where S_i is the Sørensen–Dice similarity coefficient at the linear index i, and n_{max} is the total length of the linearized list of spike events (Fig. S5c).

$$SI = \frac{1}{n_{max}} \sum_{i=1}^{n_{max}} [S_i > 0.25] \qquad where\ [P] = \begin{cases} 1\ if\ P\ is\ true, \\ 0\ if\ P\ is\ false; \end{cases} \#(4)$$

Mitochondria tracking

We measured mitochondrial dynamics through computing the average velocity (v_{avg}), total distance traveled (L_{total}) within a limited time frame, and diffusion behavior based on mean square displacement (MSD). Image sequences were imported into ImageJ for photobleaching correction and background

subtraction. A rolling-ball parabola algorithm was used to correct video stacks. Afterward, mitochondria dots were tracked using ImageJ TrackMate (LOG detector, 1 µm blob diameter) and exported as .xml files. All tracks were analyzed using custom MATLAB scripts previously described[32]. Briefly, the MATLAB script excludes track data that were extracted for time frames shorter than 36 s. It then generates star plots of all tracks, computed the *MSD* (Eqn. 5)[38], L_{total} (Eqn. 6)[32], and v_{avg} (Eqn. 7)[32]. Final data was binned for each multi-curvature region within the micropatterns.

$$MSD = \frac{1}{p-\tau}\sum_{\tau=1}^{p-\tau}\left|\begin{pmatrix} x_{i+1} \\ y_{i+1} \end{pmatrix} - \begin{pmatrix} x_i \\ y_i \end{pmatrix}\right|^2 \#(5)$$

$$L_{total} = \sum_{i=1}^{p} L_i \#(6)$$

$$V_{avg} = \frac{1}{p}\sum_{i=1}^{p}\frac{L_i}{t_i - t_{i-1}} \#(7)$$

Statistical analysis

All resulting computational data was subjected to a Normality test. If normal data distribution was rejected ($p > 0.05$), non-parametrized statistical tests were used to assess significance. Spike rates of calcium events and synchronous calcium network activity were compared across devices (*L*-I, *L*-II, control) using the Mann-Whitney test and visualized based on $p > 0.05$ (not significant) and $p \leq 0.05$ (significant difference). Agarose concentration distributions were tested using appropriate one-way ANOVAs test routines ($p < 0.01$).

Results and discussion:

Stable replication of multi-scale curvatures in hydrogel-based micropatterns for neurite networks growth *in vitro*

Confined curvatures are a key feature of the cerebral tissue resulting in small and large-curved neurite growth in the human brain cortex (Fig 1a). To replicate this growth characteristic in neurite networks *in vitro* in a reproducible and highly parallelizable way, we designed six individual multi-ring patterns ranging from 280 µm (the smallest outer diameter) to 600 µm (the largest outer diameter, Fig. 1b-1e). Within the six multi-ring patterns, a set of two has identical growth widths of 10 µm, 20 µm, and 50 µm denoted as *S, M, L,* respectively (Fig. 1d). The six multi-ring patterns were assembled into four arrays and imprinted in a 3% (w/v) agarose-based hydrogel layer to generate 50 µm tall neurite growth barriers (Fig.

S1). The agarose barriers are either 15 or 25 μm denoted as I or II, respectively (Fig. 1d). The integrity of the agarose hydrogel (swelling) was tested for 48 h in culture media using fluorescent beads (Fig. S2), and the stability of agarose barriers was monitored over 12 days with neurite network forming neurons (Fig. S3). Throughout the fabrication process (Fig 2a, 2b), we found that agarose maintained high batch consistency, similar to other studies using soft-gel microstructures for patterned cell growth[28, 30, 39]. Seeded cortical neurons integrated into the microchannels between the agarose barrier and grew in circular patterns forming arced neurite networks over 12 DIV (Fig 2c1-c2, Fig S3b). Lastly, we measured the total growth coverage of seeded cells in the multi-curvature patterns (Fig 2d and 2e). Based on a percentage growth area coverage (cells per ring area), we found that growth coverage decreased with increasing curvature (k1 = smallest, k4 = largest, Fig 2e). The maximum growth did not exceed 30% of the total area for any curvature values ($k > 0.004\ \mu m^{-1}$). These findings remained consistent within two individual designs with different agarose barriers (width = 20 μm, 25 μm) and identical cell growth patterns (width = 50 μm) and further confirm the growth inhibition effect under large curvatures ($k > 0.1\ \mu m^{-1}$) shown by Roth *et al.*[25]

In summary, the micropatterned hydrogel substrates allow primary cortical neurons to grow neurite networks in multi-curvature micropatterns ranging from $0.003\ \mu m^{-1}$ to $0.2\ \mu m^{-1}$ in a stable and reproducible manner and provides the foundation for a parallelized analysis of neuronal cell signaling and intracellular transport dynamics.

Static Ca^{2+} levels change under distinct multi-curvature patterns

To investigate spatial differences in static calcium levels relying on unique micro-curvature patterns, we extracted static normalized fluorescent calcium profiles from Fluo-4 AM stained mature grown neurite networks (rat, E18, cortical neurons, 9 – 12 DIV). We measured the curvature effects in relation to static calcium intensity levels with all circular variation types (Fig. 3a1-a3) using semi-coded scripts (Fig. 3b1-b4, Fig. S4). When comparing static calcium profiles between unpatterned neuronal network growth and multi-curvature-based micropatterns, we observed distinct shifts in calcium amplitude depending on the curvature region (Fig. 3c1-c3). As expected, the unpatterned network reveals an almost uniform calcium distribution (Fig. 3c2). However, the micropatterned network shows spatial differences in the amplitude of the calcium profile depending on the curvature (Fig. 3c3). This trend is further supported by comparing normalized calcium fluorescent profiles between the six different multi-ring patterns (Fig. 3d1-d3). Interestingly, three major static calcium profiles seem to emerge from the multi-curvature patterns. If the growth ring width, where the neuronal cells adhere, is below 50 μm, the bent neurites seem to either show large intensity amplitudes above the average intensity for very large curvatures ($k > 0.1\ \mu m^{-1}$) or attenuated amplitudes within $0.01\ \mu m^{-1}$ to $0.05\ \mu m^{-1}$ (Fig. 3d1, 3d2, 3e1, 3e2), independent of the smaller

barrier widths (*S&M-I*:15 μm versus *S&M-II*:25 μm). If the growth ring width is above 50 μm, neurite networks still grow circularly; however, the static calcium profiles appear to be as uniformly distributed as for unpatterned neurite networks (Fig. 3d3, 3e3). These observations may be explained through metabolic signaling between the multi-curvature rings, which can still occur through the agarose barriers due to the porosity of agarose[26, 40]. Furthermore, the higher calcium intensity levels under larger curvatures ($k > 0.1\ \mu m^{-1}$) may indicate the activation of an environmental cue due to mechanical forces, which have been linked in previous studies to cause a Ca^{2+} influx in cortical neurons[33, 41-44]. In summary, our results suggest that varying degrees of curvatures may affect static calcium profiles distinctively in neuronal tissues.

Ca^{2+} event rates show sensitivity to multi-scaled curvature patterns

To understand the impact of curvature on calcium signaling, we monitored spontaneously evoked temporal calcium dynamics in multi-curvature neurite networks grown from cortical neurons. Based on the static calcium patterns shown before, we selected the two largest growth area devices with 50 μm growth ring width to observe temporal changes in calcium signaling compared to an unpatterned control (Fig. 4a). Transient fluorescent calcium signals were monitored using a single-wavelength Fluo-4 AM calcium indicator due to its large dynamic range[34, 36]. Increasing and decreasing cytosolic calcium levels were decomposed using custom software that located individual somata as regions of interest (ROIs) and categorized the ROIs based on the curvature range in which they resided (Fig. S5). Figures 4c1 to 4c3 show a representative example of calcium transient and its rate of change over a 30 s time-window based on a slow-scanning speed (2 Hz). With increasing curvature, cortical neurons showed reduced transient calcium signaling activity, as shown in the calcium raster plots (Fig. 4b) and a decrease in spike rates of calcium events (Fig. 4d1-d2) in contrast to randomized network growth (Fig. 4d3). From the raster plot, we then extracted an average calcium event rate of 0.54 spike events min^{-1} for the 15 μm barrier width and 0.35 spike events min^{-1} for the 25 μm barrier width. In contrast to the multi-curvature patterns, unpatterned networks had an average calcium event rate of 0.67 spikes min^{-1}. We attribute the similar spike rate between the unpatterned and the multi-curvature pattern with the lower agarose barrier width and potential transport of signaling molecules that can diffuse through the agarose pores[40]. Agarose barriers above 25 μm may potentially decouple and therefore desynchronize neurite network patterns, reducing the overall spike rate of calcium events.

Multi-curvature patterns based on thicker agarose barriers uncouple Ca^{2+} event synchronicity

The synchronous activity of spontaneously occurring calcium events has been shown for cortical neuron aggregates *in vitro*[37, 45-47]. Here, we analyzed if the multi-curvature pattern also induced spontaneous

synchronous calcium events. We computed the Sørensen–Dice coefficient from the ROI spike trains at each curvature range to test the synchronicity of calcium events in the multi-curvature patterns. A total synchronicity index (SI) for the individually curved cortical networks then indicates high synchronous calcium events within the network when more than 25% of the events occurred in the same time interval (Fig. 4e1-e3, Fig. S5). Multi-curvature micropatterns with 15 μm agarose barrier width showed the highest synchronicity in calcium events and highest variability across the different curvatures with a mean SI of 0.106 (Fig. 4e1). Multi-curvature patterns with 25 μm agarose barrier width reduced the mean SI to 0.077; however, more distinct regions of SI's are observed based on distinct curvature regions suggesting an uncoupling of calcium event synchronicity between the distinct curvatures (Fig. 4e2).
In contrast to the multi-curvature patterns, unpatterned neurite networks had a low mean SI of 0.039 without distinct regional differences (Fig. 4e3, Mann-Whitney $p<0.05$). This asynchronous signaling effect is also confirmed without binning the data set by curvature (kn). No significantly different synchronicity was observed (Fig. 4e3, Mann-Whitney $p<0.05$) between the artificial regions in the unpatterned network. This observation could mean that the multi-curvature patterns show more mature neurite network development than the unpatterned networks[45, 48, 49]. On a side note, we want to add here that our spike event detection result from slow scanning calcium imaging (2 Hz). This approach makes the computation of the synchronicity index specifically robust; however, our calcium transients may disguise a high true spike rate of calcium events[50] or may include calcium signal contamination from non-neuronal cells[6]. In summary, micropatterning neuronal growth under distinct curvatures and with varying hydrogel barrier widths enables the formation of distinct neuronal network functionality, which cannot be replicated in the unpatterned growth of neurite networks.

High curvatures immobilize the transport of mitochondria

Calcium signaling and mitochondrial dynamics are highly intertwined subcellular processes in neuronal cells[51-53]. Here, we test if the modulation of calcium signals through the multi-curvature growth pattern of neurite networks also influence mitochondria transport dynamics[53-60]. Distinct mitochondria staining is noted based on the neurite network growth with and without the multi-curvature design (Fig. 5a). Using ImageJ TrackMate[61] and custom coded MATLAB scripts[32], mitochondria transport (Fig. 5b) was characterized based on mean-square displacement (MSD, Fig. 5c), center plots of trajectories (Fig. 5d), and average velocity (Fig. 5e). We found that low curvature values, $0.003 < k < 0.01$ μm^{-1} showed convection-driven mitochondria transport with a preferred direction (Fig. 5c and 5d). Additionally, we see that these lower curvature ranges reveal two distinct velocity clusters (mean1 = 0.15 μm/s and mean2 = 0.77 μm/s, Fig. 5e). These velocity ranges are typical for mitochondria docking and diffusive behavior[52, 55, 58] versus active transport behavior previously shown between 0.55 μm/s and 0.61 μm/s[52, 58, 62]. In high-

curvature ranges ($0.01 < k < 0.2\ \mu m^{-1}$), we observed no active transport behavior. Neurons growing in unpatterned neurite networks show mitochondria velocities closely related to previously established mitochondria velocities *in vitro* neuronal cultures[52, 55, 59, 63]. Similar to Chang *et al.*[56], mitochondria dynamics in our experiments show both stationary and high mobile events (Fig. 5e).
In summary, while both the lower curvature micropatterns and the unpatterned neurite networks showed stationary docking and active transport behavior for mitochondria, the high curvatures immobilize these dynamic events. These stationary mitochondria dynamics may be attributed to increased mechanical stress or may be needed to buffer the local increase of intracellular cytosolic calcium[64].

Mechanically shaping the Ca^{2+} mitochondria axis in neuronal network growth

In our experimental data, we observed two distinct patterns of mitochondria dynamics and calcium signaling events, depending on either high or low arcs in our multi-curvature patterns. Figure 6 summarizes our experimental findings and sets them into the context of a calcium-mediated mitochondria recruitment hypothesis, which shows a dominant feature depending on the strength of curvature range. Under high curvatures ($k > 0.01\ \mu m^{-1}$), cortical neuronal networks show higher stationary calcium levels but lower mitochondria transport velocity and lower spike rate dynamics (Fig. 4d1-d2, Fig. 6a, Fig. S6). In contrast, low curvature ranges promoted high mitochondria dynamics and lower stationary calcium signals at slightly higher spike rate dynamics (Fig. 4d1-d2, Fig. 6a, Fig. S6). These results show not only a differential image in comparison to the control data, but they also seem to allow us to finetune regulatory events in neurite networks based on precisely controllable mechanical growth cues based on curvatures. The interplay of Ca^{2+} and mitochondria is well recognized with cellular energy production[53], cell fate regulation[65], and cellular homeostasis[51]. As dynamic organelles, mitochondria are responsive to both environmental and physiological cues[58, 62]. Additionally, it has been proposed that elevated Ca^{2+} influx limit mitochondrion mobility[57, 66]. This reduced mobility may indicate elevated calcium levels due to higher curvature levels in the patterns. There has also been an interest in regulating mechanosensitive Ca^{2+} channels in neurons to elucidate the role mechanosensitivity plays in Ca^{2+} signaling and its downstream processes[67]. Calabrese et al. observed that temporary membrane stretching accelerated the development of Ca^{2+} currents, amplifying the net Ca^{2+} entry[68]. This net influx was further confirmed when Kunze and Tay et al. observed Ca^{2+} influx during tugging of cell membrane-localized magnetic nanoparticles[33]. Interestingly, Muqing et al. observed both the arrest of mitochondrial transport during increased cytosolic Ca^{2+} and a consecutive increase in mitochondrial calcium[60], which further substantiated the hypothesis of mitochondrial recruitment at increased local Ca^{2+}. Hence, we hypothesize that the higher curvatures exhibited in our device create a physical environment capable of continuously stretching mechanosensitive Ca^{2+} channels, creating locally increased Ca^{2+} levels that locally recruit

mitochondria for docking (Fig. 6b, Fig. S6). Therefore, the decrease in mitochondrial velocity rates can be seen as a downstream consequence of increased internal Ca^{2+} concentrations at greater curvatures.

Conclusions

In summary, we have developed a reproducible micropatterning method to design multi-curvature neuronal network growth in groves of agarose hydrogels. Using these multi-curved neurite networks, we observed distinct calcium signaling and mitochondria transport events. We revealed that high curvatures ($k > 0.01\ \mu m^{-1}$) favor dynamic calcium and transport events rather than stationary events in comparison to low curvature ranges ($k < 0.01\ \mu m^{-1}$). We also demonstrated that incorporating soft-gel microchannels into neuronal cell assays is a versatile, low-cost, and highly reproducible method to control neurite network growth under confined curvatures. Broadly, our multi-curvature-based soft-embossing of micropatterns allows for rapid and relatively easy reproducibility in studying confined curvatures associated with mechanical cues imposed on neuronal cell growth in the highly folded landscape of the human cerebral cortex. Although projected to a flat surface, where neuronal cells grow, the quasi three-dimensional environment due to the hydrogel barriers makes it specifically compatible with standard live-cell fluorescent microscopy techniques. Furthermore, the micropatterning approach makes multi-curvature studies accessible for large-scale pharmaceutical testing and neurobiology studies. Our highly parallelized design enables automated image acquisition, parallelized batch processing, scaling up experimental batch size while being compatible with standard cell culture assays. Beyond calcium signaling and mitochondria dynamics, our multi-curvature patterns can bring further insights into functional changes imposed to neuronal networks through the cortical folded landscape.

Conflicts of interest

The authors declare to have had no competing financial or any other conflicts of interest during the duration of this study.

Acknowledgments

AK received a National Science Foundation CAREER award (Grant# CBET-1846271). HK was supported through an INBRE fellowship funded by the National Institute of General Medical Sciences of the NIH (P20GM103474). This work was performed in part at the Montana Nanotechnology Facility, a member of the National Nanotechnology Coordinated Infrastructure (NNCI) supported by the National Science Foundation (Grant# ECCS-1542210).

Author Contributions

CB designed the multi-curvature micropatterns. HK fabricated the hydrogel-based cell assay and performed cell culture experiments. HK, CB, and AK designed and analyzed the cell culture experiments. AK conceptualized, designed, and supervised the study. All authors wrote and revised the manuscript.

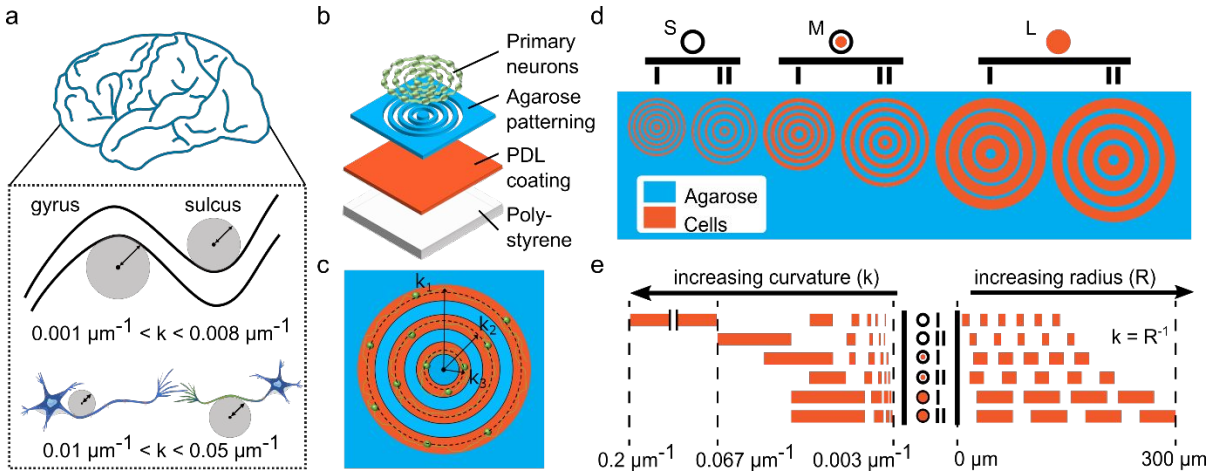

Figure 1. Low-cost, multi-curvature micropatterning design for calcium-based neuronal network studies. a) In-vivo representation of diverse arc ranges occurring in the human cerebral cortex. Low curvatures ($k < 0.008\ \mu m^{-1}$) are determined by gyrus and sulcus structures. High curvatures ($k > 0.01\ \mu m^{-1}$) are determined through bended neurite/axonal growth characteristics. b-c) Experimental design of micro-patterned multi-curvature-based growth of primary cortical neurons (E18, rat model) on polystyrene substrates using hydrogel boundaries in b) exploded view, c) top view. d) Six different multi-curvature micro patterns used in this study. Letters indicate cell growth width. S: small (10 μm), M: middle (20 μm), L: large (50 μm). e) Side view of panel d shows radius and curvature parameters associated with the six different designed micropatterns in panel d.

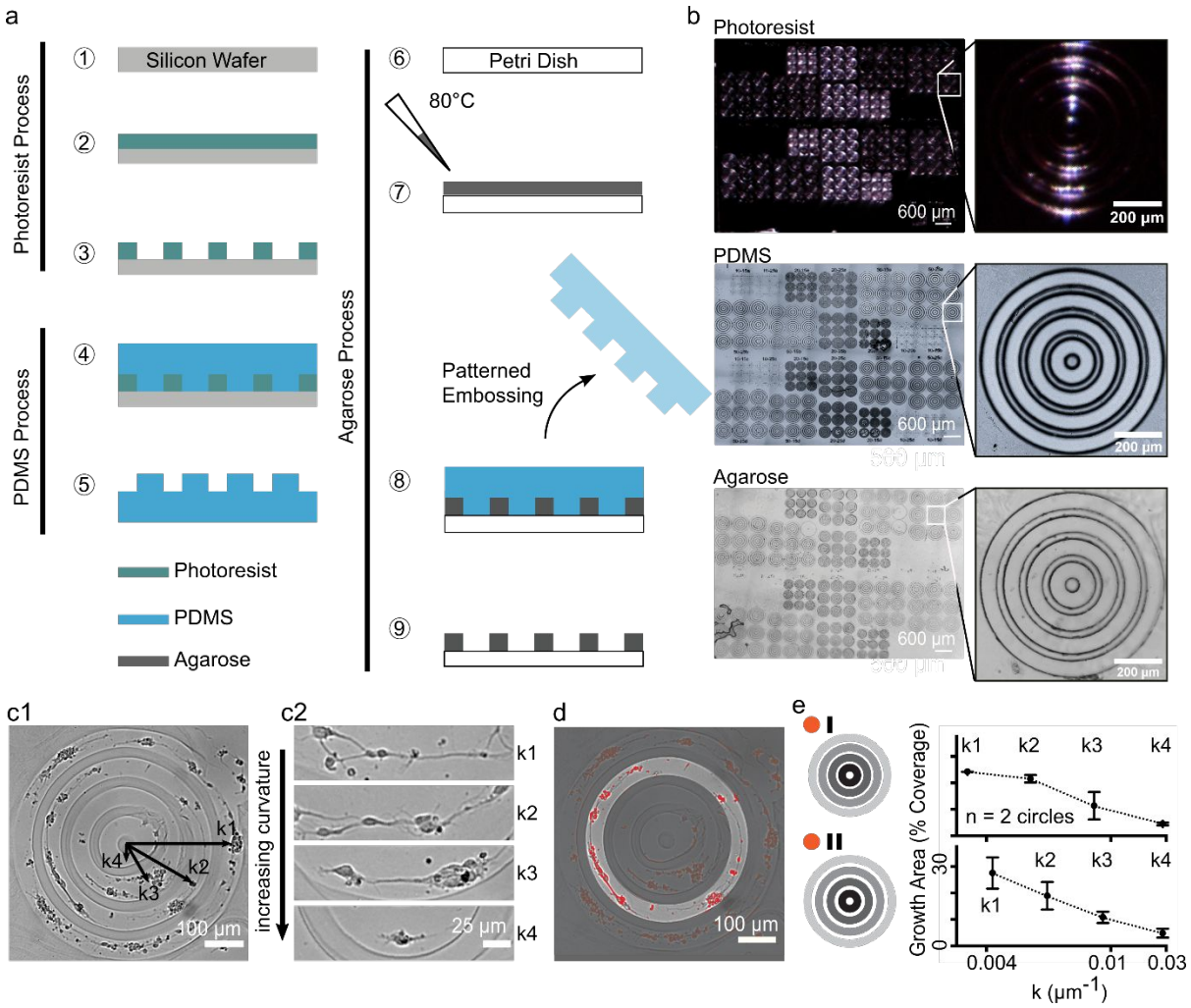

Figure 2. Device design shows the robust fabrication of curvature features and embedded curved neurite outgrowth. (a) Schematic of micropatterning process flow. The photoresist process takes place in the cleanroom and yields a modeling master. The process of polydimethylsiloxane (PDMS) stamp formation is repeatable and done in a physical wet lab setting. The last process uses liquified agarose hydrogel as a base layer onto which the PDMS microstructures get imprinted. This step yields the multi-curvature hydrogel patterns where neuronal cells grow within the grooves. (b) Microscope images show the photoresist structure on the master, the microstructures after being cast into PDMS, and the imprinted hydrogel microstructures. (c1 and c2) DIC images of day 12 cortical neurons forming circular networks in the multi-layered curvatures. Distinct curved growth patterns depend on curvatures k1, k2, k3, and k4, where k1 is always the smallest curvature. (d) Image processing mask used to extract curvature-dependent static and transient calcium activity within one circular network. (e) The diagram shows curvature-dependent coverage of total ring growth area in the micropatterns, extracted from two patterns (n = 2, each) at 12 DIV. The covered growth area decreases as curvature increases.

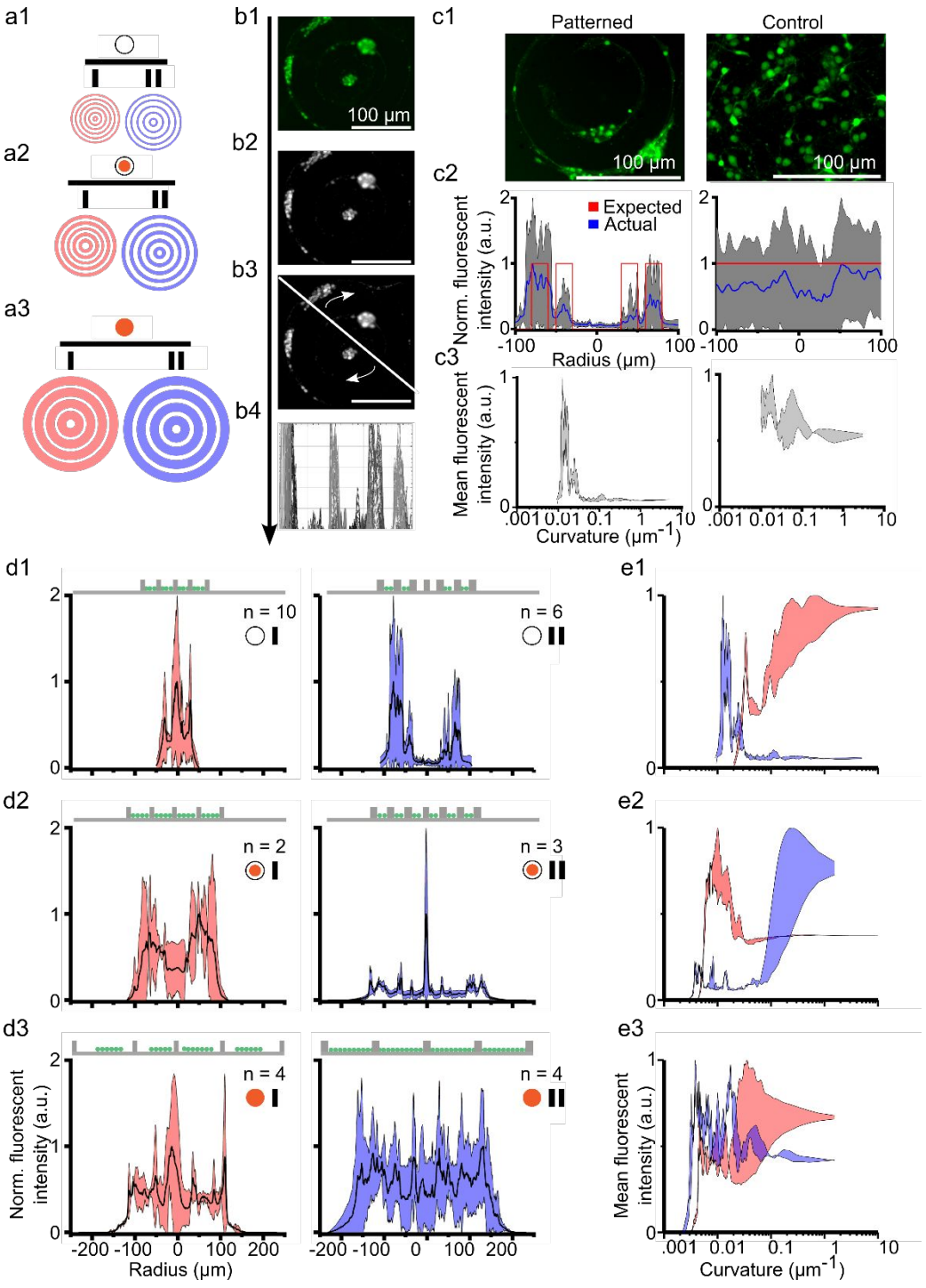

Figure 3. Multi-curvature patterns reveal distinct characteristics in static calcium fluorescence in two-week-old circular neurite networks (rat, E18). (a1-a3) The six distinct multi-curvature micropattern designs. The colored area is the neuronal cell growth area. Red: Constant agarose barrier width = 15 µm. Blue: Constant agarose barrier width = 25 µm. (b1-b4) Image processing workflow of raw calcium

images. (b1) Original 12-bit false-color green-fluorescent calcium images (Fluo4 AM). (b2) Down sampled 8-bit gray-scale image after background subtraction. (b3) Automated circular calcium profiling captures fluorescent intensity profile across one individual micropattern design. (b4) Raw plots of the fluorescent intensity profiles for every single pattern. (c1) Representative fluorescent image of a patterned and unpatterned (control) cortical neuron culture (E18, rat, 12 DIV), respectively. (c2) Normalized fluorescent profiles show distinct static calcium characteristics corresponding to panel c1. The fluorescent signal was normalized over its average (mean intensity). (c3) The mean intensity of the fluorescent signal was plotted over the curvature. (d1-d3) Normalized fluorescent profiles depending on the six distinct micro-patterns. (e1-e3) Mean fluorescent intensity profile plots correlated with patterned curvatures.

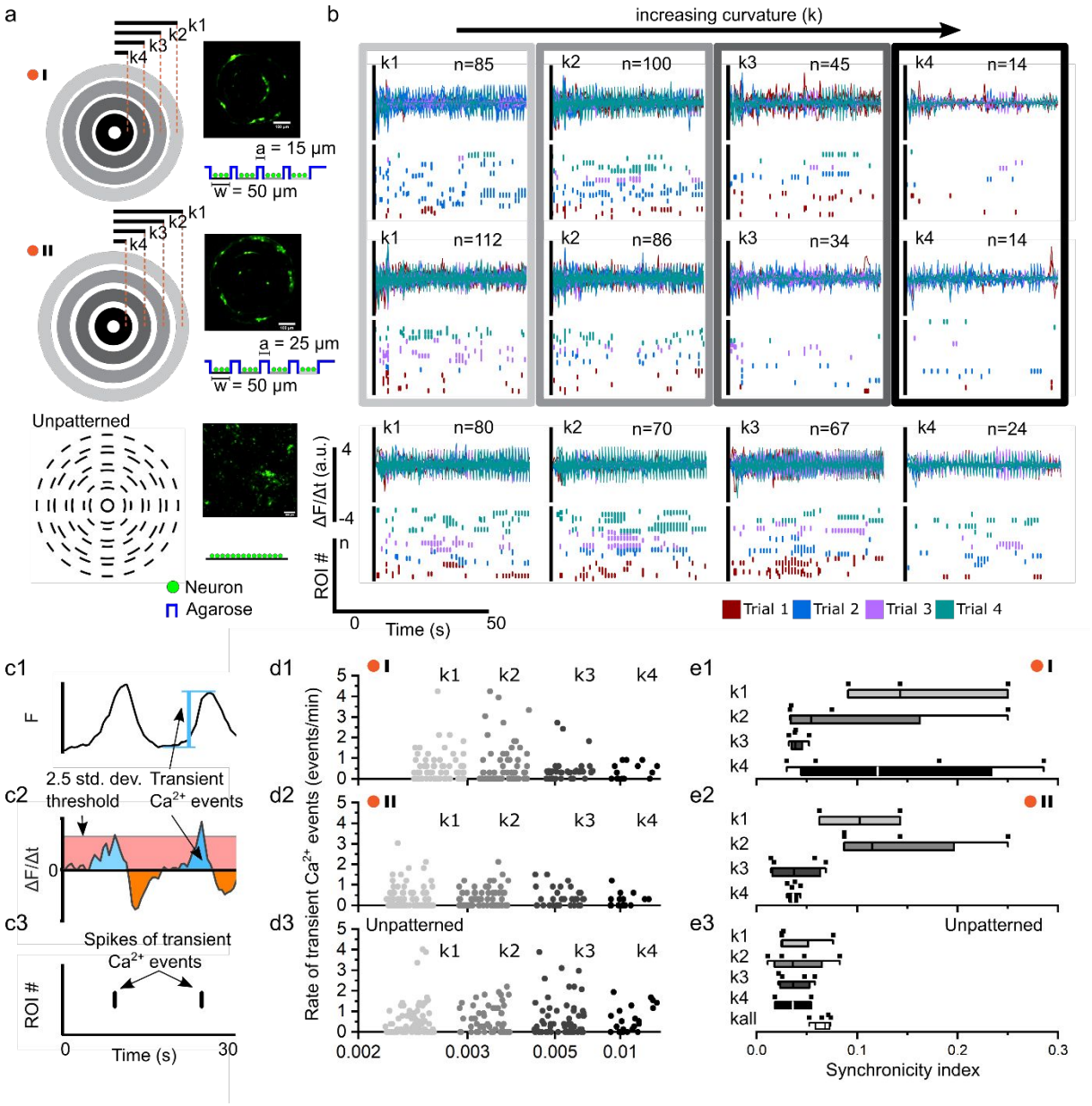

Figure 4. Transient calcium signaling in neurite networks grown in multi-curvature patterns is curvature dependent. (a) Schematic highlights the top-view and side-view of two selected multi-curvature patterns, and the control, with associated representative green fluorescent images (Fluo-4 AM) and shows primary cortical neurons at 12 DIV (E18, rat). The gray-shaded area is the neuronal cell growth area with agarose barrier width = 15 μm and 25 μm. (b) Time-varying plots show calcium dynamics based on continuous fluorescence and raster spike plots associated with the selected patterns from (a). (c1 – c3) Fluorescent signal processing for extracting spikes of calcium events, where F is the time-variant fluorescent signal extracted from calcium imaging, ΔF/Δt is the relative rate of change in cytosolic calcium, and threshold-based calcium events are denoted as spikes in individual cell bodies

(regions of interests = ROIs). K1 – k4 labels indicate different curvature rings, with k1 being the smallest curvature. (d1 – d2) Density plots indicate relative spike events per minute for neurons growing in distinct curvatures. For the unpatterned control, the same curvature mask was used to extract region-specific calcium events. (e1 – e3) Boxplots show the distribution of synchronous calcium spike activity associated with the distinct curvature regions.

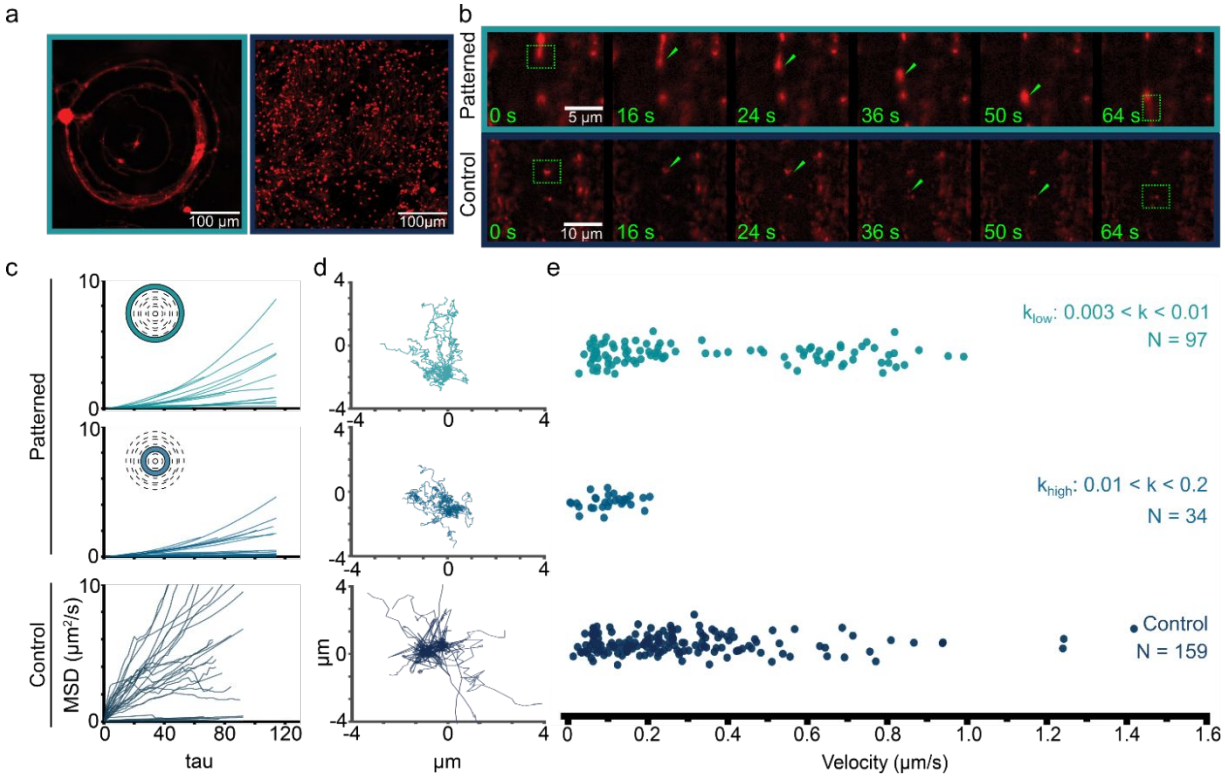

Figure 5: Strong curvature bends slow down mitochondria movement. (a) Representative fluorescent images show red fluorescent-labeled mitochondria (MitoTracker) in primary cortical neuron cultures (12 DIV, E18, rat) in the multi-curvature patterns and the unpatterned culture environment (control). (b) Time-lapse image sequence presents the mitochondrial movement in two-week-old living neurons. The green arrowhead points to a particular mitochondrion of interest and its moving position over time extracted from circular (top) and unpatterned = control (bottom) neural growth. (c) Mean-square displacement (MSD) plots were computed for N individual mitochondria tracks selected from distinct low (k_{low}), high (k_{high}) curvature regions, or the unpatterned no curvature influence control region. (d) Center plots of mitochondria trajectories associated with distinct curvature regions and control. (e) Distribution of average velocity for individual mitochondria associated with the distinct low and high curvature region versus the unpatterned control condition.

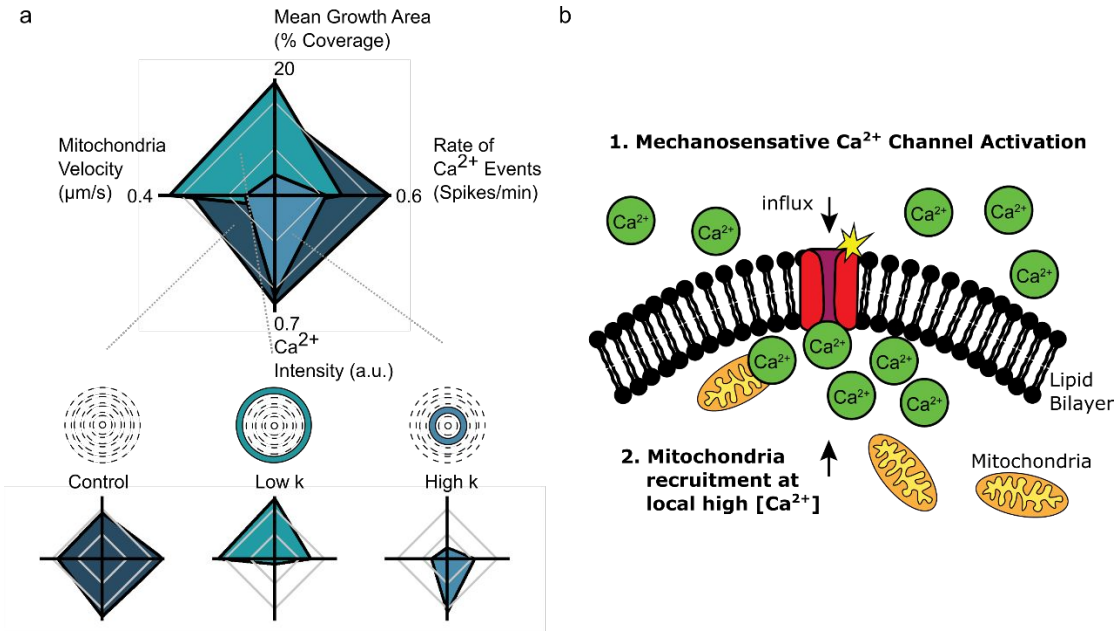

Figure 6: Confined curvature microenvironments reveal distinct fingerprints based on static and transient Ca^{2+} signaling events, mean growth area, and mitochondrial movement dynamics. (a) A four-axis radar chart compares the maximum spike rate, maximum static average calcium intensity, maximum average mitochondria velocity, and the maximum mean growth area between the curvatures and unpatterned culture conditions. (b) Schematic of a possible mechano-activated mitochondrial recruitment hypothesis, where (1) mechanosensitive Ca^{2+} channels are activated due to strong mechanical bending of the neuronal cell membrane (neurite), which potentially leads to (2) mitochondria recruitment due to a local levitation of cytosolic Ca^{2+}, which then reduces mitochondria transport velocities.

References:

1. B. Fischl, N. Rajendran, E. Busa, J. Augustinack, O. Hinds, B. T. T. Yeo, H. Mohlberg, K. Amunts and K. Zilles, *Cereb. Cortex*, 2008, **18**, 1973-1980.
2. K. Im, J.-M. Lee, O. Lyttelton, S. H. Kim, A. C. Evans and S. I. Kim, *Cereb. Cortex*, 2008, **18**, 2181-2191.
3. T. Tallinen, J. Y. Chung, J. S. Biggins and L. Mahadevan, *Proceedings of the National Academy of Sciences*, 2014, **111**, 12667.
4. L. Ronan, R. Pienaar, G. Williams, E. Bullmore, T. J. Crow, N. Roberts, P. B. Jones, J. Suckling and P. C. Fletcher, *Int J Neural Syst*, 2011, **21**, 351-366.
5. C. Ecker, L. Ronan, Y. Feng, E. Daly, C. Murphy, C. E. Ginestet, M. Brammer, P. C. Fletcher, E. T. Bullmore, J. Suckling, S. Baron-Cohen, S. Williams, E. Loth and D. G. M. Murphy, *Proceedings of the National Academy of Sciences*, 2013, **110**, 13222-13227.
6. Y. Ikegaya, M. Le Bon-Jego and R. Yuste, *Neuroscience Research*, 2005, **52**, 132-138.
7. S.-M. Yu, J. M. Oh, J. Lee, W. Lee-Kwon, W. Jung, F. Amblard, S. Granick and Y.-K. Cho, *Acta Biomaterialia*, 2018, **77**, 311-321.
8. D. Marrone, *Brain Research Reviews*, 2002, **38**, 291-308.
9. N. L. Voets, B. C. Bernhardt, H. Kim, U. Yoon and N. Bernasconi, *Neurology*, 2011, **76**, 138.
10. C. W. Nordahl, D. Dierker, I. Mostafavi, C. M. Schumann, S. M. Rivera, D. G. Amaral and D. C. Van Essen, *J. Neurosci.*, 2007, **27**, 11725-11735.
11. A. Y. Hardan, R. J. Jou, M. S. Keshavan, R. Varma and N. J. Minshew, *Psychiatry Res. Neuroimaging*, 2004, **131**, 263-268.
12. J. M. Harris, P. Miller, E. C. Johnstone and S. M. Lawrie, *Schizophr. Res.*, 2004, **67**, 26-26.
13. J. J. Wisco, G. Kuperberg, D. Manoach, B. T. Quinn, E. Busa, B. Fischl, S. Heckers and A. G. Sorensen, *Schizophr. Res.*, 2007, **94**, 317-327.
14. K. Wagstyl, L. Ronan, K. J. Whitaker, I. M. Goodyer, N. Roberts, T. J. Crow and P. C. Fletcher, *Translational Psychiatry*, 2016, **6**, e780-e780.
15. C. C. Hilgetag and H. Barbas, *PLoS Computational Biology*, 2006, **2**, e22.
16. L. J. Millet, M. E. Stewart, J. V. Sweedler, R. G. Nuzzo and M. U. Gillette, *Lab on a Chip*, 2007, **7**, 987-994.
17. M. Park, E. Oh, J. Seo, M.-H. Kim, H. Cho, J. Y. Choi, H. Lee and I. S. Choi, *Small*, 2016, **12**, 1148-1152.
18. N. M. Dowell-Mesfin, M. A. Abdul-Karim, A. M. P. Turner, S. Schanz, H. G. Craighead, B. Roysam, J. N. Turner and W. Shain, *Journal of Neural Engineering*, 2004, **1**, 78-90.
19. R. M. Smeal and P. A. Tresco, *Experimental Neurology*, 2008, **213**, 281-292.
20. R. M. Smeal, R. Rabbitt, R. Biran and P. A. Tresco, *Annals of biomedical engineering*, 2005, **33**, 376-382.
21. L. Micholt, A. Gärtner, D. Prodanov, D. Braeken, C. G. Dotti and C. Bartic, *PLOS ONE*, 2013, **8**, e66170.
22. D. Y. Fozdar, J. Y. Lee, C. E. Schmidt and S. Chen, *Biofabrication*, 2010, **2**, 035005.
23. A. Vishwanathan, G.-Q. Bi and H. C. Zeringue, *Lab on a Chip*, 2011, **11**, 1081-1088.
24. S. R. Hart, Y. Huang, T. Fothergill, D. C. Lumbard, E. W. Dent and J. C. Williams, *Lab on a Chip*, 2013, **13**, 562-569.
25. S. Roth, M. Bisbal, J. Brocard, G. Bugnicourt, Y. Saoudi, A. Andrieux, S. Gory-Fauré and C. Villard, *PLOS ONE*, 2012, **7**, e33623.
26. A. Kunze, M. Giugliano, A. Valero and P. Renaud, *Biomaterials*, 2011, **32**, 2088-2098.
27. N. Tanaka, T. Yamashita, A. Sato, V. Vogel and Y. Tanaka, *PLOS ONE*, 2017, **12**, e0173647.
28. G. Kang, J. H. Lee, C. S. Lee and Y. Nam, *Lab Chip*, 2009, **9**, 3236-3242.
29. J. M. Vensi Basso, I. Yurchenko, M. Simon, D. J. Rizzo and C. Staii, *Physical Review E*, 2019, **99**, 022408.
30. S. Kobel, M. Limacher, S. Gobaa, T. Laroche and M. P. Lutolf, *Langmuir*, 2009, **25**, 8774-8779.
31. C. L. Beck, C. J. Hickman and A. Kunze, *Scientific Reports*, 2020, **10**, 12568.
32. A. Kunze, C. T. Murray, C. Godzich, J. Lin, K. Owsley, A. Tay and D. Di Carlo, *Lab on a Chip*, 2017, **17**, 842-854.
33. A. Tay, A. Kunze, C. Murray and D. Di Carlo, *ACS Nano*, 2016, **10**, 2331-2341.
34. J. T. Lock, I. Parker and I. F. Smith, *Cell Calcium*, 2015, **58**, 638-648.
35. C. Grienberger and A. Konnerth, *Neuron*, 2012, **73**, 862-885.
36. K. R. Gee, K. A. Brown, W. N. U. Chen, J. Bishop-Stewart, D. Gray and I. Johnson, *Cell Calcium*, 2000, **27**, 97-106.
37. Y. Ikegaya, G. Aaron, R. Cossart, D. Aronov, I. Lampl, D. Ferster and R. Yuste, *Science*, 2004, **304**, 559-564.

38. N. Monnier, S.-M. Guo, M. Mori, J. He, P. Lénárt and M. Bathe, *Biophysical Journal*, 2012, **103**, 616-626.
39. M. J. Jang and Y. Nam, *Macromol. Biosci.*, 2015, **15**, 613-621.
40. A. Pluen, P. A. Netti, R. K. Jain and D. A. Berk, *Biophysical Journal*, 1999, **77**, 542-552.
41. P. A. Janmey and C. A. McCulloch, *Annual Review of Biomedical Engineering*, 2007, **9**, 1-34.
42. A. Soloperto, A. Boccaccio, A. Contestabile, M. Moroni, G. I. Hallinan, G. Palazzolo, J. Chad, K. Deinhardt, D. Carugo and F. Difato, *Journal of Cell Science*, 2018, **131**, jcs210393.
43. R. D. Burgoyne, *Nature Reviews Neuroscience*, 2007, **8**, 182-193.
44. M. Chighizola, T. Dini, C. Lenardi, P. Milani, A. Podestà and C. Schulte, *Biophysical Reviews*, 2019, **11**, 701-720.
45. T. Murphy, L. Blatter, W. Wier and J. Baraban, *The Journal of Neuroscience*, 1992, **12**, 4834-4845.
46. P. Uhlhaas, G. Pipa, B. Lima, L. Melloni, S. Neuenschwander, D. Nikolić and W. Singer, *Frontiers in Integrative Neuroscience*, 2009, **3**.
47. Y. Ikegaya, M. Le Bon-Jego and R. Yuste, *Neurosci Res*, 2005, **52**, 132-138.
48. G. Shahaf and S. Marom, *The Journal of Neuroscience*, 2001, **21**, 8782-8788.
49. E. Maeda, H. Robinson and A. Kawana, *The Journal of Neuroscience*, 1995, **15**, 6834-6845.
50. T. Deneux, A. Kaszas, G. Szalay, G. Katona, T. Lakner, A. Grinvald, B. Rózsa and I. Vanzetta, *Nature Communications*, 2016, **7**, 12190.
51. V. Paupe and J. Prudent, *Biochem Biophys Res Commun*, 2018, **500**, 75-86.
52. R. F. Niescier, S. K. Kwak, S. H. Joo, K. T. Chang and K.-T. Min, *Frontiers in Cellular Neuroscience*, 2016, **10**.
53. L. Contreras, I. Drago, E. Zampese and T. Pozzan, *Biochimica et Biophysica Acta (BBA) - Bioenergetics*, 2010, **1797**, 607-618.
54. M. Miragoli, Jose L. Sanchez-Alonso, A. Bhargava, Peter T. Wright, M. Sikkel, S. Schobesberger, I. Diakonov, P. Novak, A. Castaldi, P. Cattaneo, Alexander R. Lyon, Max J. Lab and J. Gorelik, *Cell Reports*, 2016, **14**, 140-151.
55. Z.-H. Sheng, *The Journal of Cell Biology*, 2014, **204**, 1087-1098.
56. D. T. W. Chang and I. J. Reynolds, *Neuroscience*, 2006, **141**, 727-736.
57. D. T. W. Chang, A. S. Honick and I. J. Reynolds, *J. Neurosci.*, 2006, **26**, 7035-7045.
58. P. J. Hollenbeck and W. M. Saxton, *Journal of cell science*, 2005, **118**, 5411-5419.
59. K. E. Miller, *Journal of Cell Science*, 2004, **117**, 2791-2804.
60. M. Yi, D. Weaver and G. Hajnóczky, *The Journal of cell biology*, 2004, **167**, 661-672.
61. J.-Y. Tinevez, N. Perry, J. Schindelin, G. M. Hoopes, G. D. Reynolds, E. Laplantine, S. Y. Bednarek, S. L. Shorte and K. W. Eliceiri, *Methods*, 2017, **115**, 80-90.
62. A. Mandal and C. M. Drerup, *Frontiers in Cellular Neuroscience*, 2019, **13**.
63. Z.-H. Sheng and Q. Cai, *Nature Reviews Neuroscience*, 2012, **13**, 77-93.
64. M.-Y. Lin and Z.-H. Sheng, *Experimental Cell Research*, 2015, **334**, 35-44.
65. D. R. Green, L. Galluzzi and G. Kroemer, *Science*, 2014, **345**, 1466-+.
66. G. L. Rintoul, A. J. Filiano, J. B. Brocard, G. J. Kress and I. J. Reynolds, *The Journal of Neuroscience*, 2003, **23**, 7881-7888.
67. B. Martinac, *Journal of Cell Science*, 2004, **117**, 2449.
68. B. Calabrese, I. V. Tabarean, P. Juranka and C. E. Morris, *Biophysical Journal*, 2002, **83**, 2560-2574.